

# Predicting the suitability of photocatalysts for water splitting using Koopmans spectral functionals: The case of TiO<sub>2</sub> polymorphs

Marija Stojkovic,<sup>1,\*</sup> Edward Linscott,<sup>2,3</sup> and Nicola Marzari<sup>1,2,3</sup>

<sup>1</sup>*Theory and Simulations of Materials (THEOS),*

*École Polytechnique Fédérale de Lausanne, 1015 Lausanne, Switzerland*

<sup>2</sup>*Center for Scientific Computing, Theory and Data,*

*Paul Scherrer Institute, 5232 Villigen PSI, Switzerland*

<sup>3</sup>*National Centre for Computational Design and Discovery of Novel Materials (MARVEL),*

*Paul Scherrer Institute, 5232 Villigen PSI, Switzerland*

(Dated: December 24, 2024)

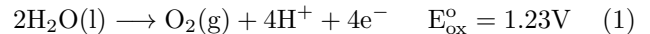
Photocatalytic water splitting has attracted considerable attention for renewable energy production. Since the first reported photocatalytic water splitting by titanium dioxide, this material remains one of the most promising photocatalysts, due to its suitable band gap and band-edge positions. However, predicting both of these properties is a challenging task for existing computational methods. Here we show how Koopmans spectral functionals can accurately predict the band structure and level alignment of rutile, anatase, and brookite TiO<sub>2</sub> using a computationally efficient workflow that only requires (a) a DFT calculation of the photocatalyst/vacuum interface and (b) a Koopmans spectral functional calculation of the bulk photocatalyst. The success of this approach for TiO<sub>2</sub> suggests that this strategy could be deployed for assessing the suitability of novel photocatalyst candidates.

## I. INTRODUCTION

One of the most pressing problems that we are currently facing is finding easy and low-cost renewable energy sources. Hydrogen production from water is one attractive option. In this process, water is decomposed by visible light into oxygen and hydrogen without the application of external potentials, as was first demonstrated by Fujishima and Honda using TiO<sub>2</sub> as an electrode [1]. Ever since, photocatalytic water splitting (PWS) has been in the spotlight as a way to produce hydrogen via renewable energy. Alongside experiments that have explored PWS at a fundamental level — from photon absorption to the production of molecular hydrogen — computational methods have aided our understanding of this process, and are particularly useful for identifying new candidate materials for catalysts. The search for an ideal photocatalytic material is still ongoing, and numerous studies have been conducted to tackle this problem, especially for semiconductor materials (see [2–7] and references therein).

To better understand the desirable properties for a candidate photocatalyst, let us first briefly revise the PWS process. Water splitting is, of course, not a spontaneous reaction: it requires an energy barrier to be overcome. One of the ways to do this is via solar irradiation. Upon light absorption, the catalyst plays a crucial role in a three-step process: 1. charge carrier generation, in which electrons are promoted from the valence to the conduction band (creating a hole); 2. charge separation of the electron-hole pair and migration to the surface of a catalyst; and 3. participation in redox reactions. The first two steps are especially dependent on the structural and electronic properties of the photocatalytic material. The

overall process is given by:



The water-splitting reaction involves the oxidation of water and reduction of hydrogen under standard conditions the value of the redox potentials — as referenced to the normal hydrogen electrode — are 1.23 V and 0 V respectively [8]. Given these potentials, the band gap of a suitable catalyst needs to be at least 1.23 eV; otherwise the electrons will not have enough energy to start the reaction. In practice, at least 1.6 to 1.8 eV are required, as a certain amount of excess energy (i.e. the so-called “overpotential”) is needed to overcome kinetic barriers and induce the hydrogen and oxygen evolution reactions on the surface of the electrode [9–11]. The band gap should not be too high either, since that would reduce the amount of visible light that the photocatalyst can harness.

However, an optimal band gap is not enough. For the PWS reaction to occur, the valence band maximum (VBM) needs to be higher than the oxidation potential of water while the conduction band minimum (CBM) needs to be lower than the hydrogen reduction potential. This ensures that the overall reaction has a negative change in Gibbs free energy, and is therefore spontaneous.

Given the importance of the band gap and the band alignment on the performance of photocatalysts, we would like to be able to computationally predict these properties. However, this is a challenging task. In computational materials science, Kohn-Sham density functional theory (KS-DFT) is ubiquitous, but its prediction

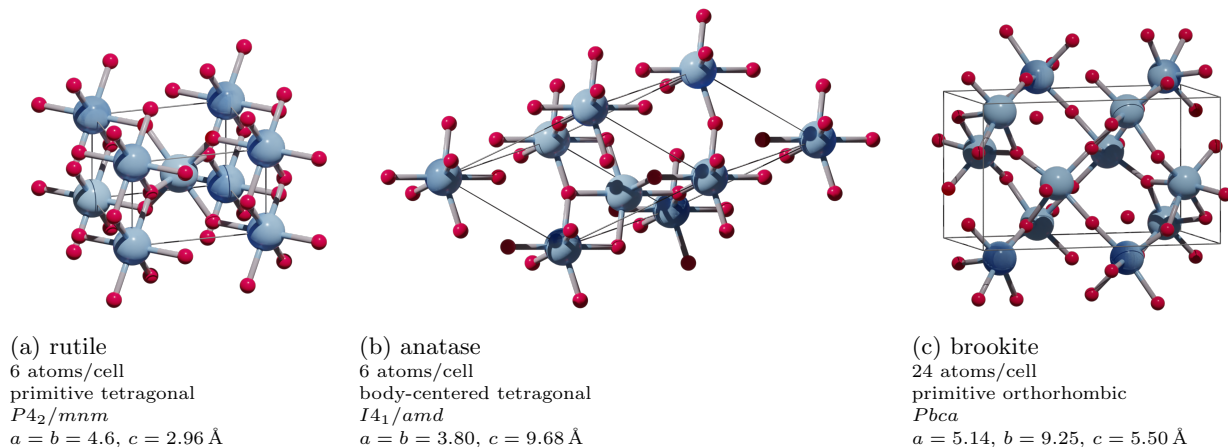


FIG. 1: Crystal structures of three  $\text{TiO}_2$  polymorphs

of band gaps and band alignment is unreliable. This failure stems from several shortcomings. Firstly, the Kohn-Sham eigenvalues (from which we obtain both the band gap and band alignment) are actually mathematical constructs and do not have a direct physical meaning — they need not correspond to genuine excitation energies of the system [12, 13]. This is true even for the exact exchange-correlation (xc) functional, for which only the highest occupied molecular orbital (HOMO) has an energy that corresponds to a physical excitation. Approximate xc functionals additionally suffer from further errors such as “one-body” self-interaction error (the incomplete cancellation of the Hartree and exchange terms for one-electron systems) [14, 15] and an erroneous curvature of the total energy with respect to the total number of particles (which should in principle be piecewise linear) [16–21]. The lack of piecewise linearity means that the eigenvalues obtained via approximate xc functionals do not match the total energy differences that one would obtain by explicitly performing electron removal/addition [16, 20, 22].

Higher-order methods have been used to overcome these shortcomings. These include hybrid functionals [16, 23–26], Hubbard and extended Hubbard functionals [27, 28], and many-body perturbation theories such as GW [29–32]. The first two approaches (partially) address the issue of piecewise linearity, but still do not have eigenvalues that can be formally interpreted as quasiparticle energies. GW, on the other hand, has formally-well-defined eigenvalues (being a theoretical framework centered on the description of quasiparticles) but (a) it is much more computationally demanding and (b) performing self-consistency does not systematically improve the results — for example, self-consistent quasiparticle GW typically overestimates band gaps and in this regard is less accurate than  $G_0W_0$  [33].

In this work we employ Koopmans spectral functionals [20] as an alternative approach that provides accurate spectral properties of materials while being less computationally demanding compared to many-body approaches.

As a test case, we apply these functionals to the three most stable polymorphs of  $\text{TiO}_2$ : rutile, anatase, and the less-studied brookite [34]. The crystal structures of these three polymorphs are presented in Figure 1.

The paper is organized as follows: in Section II we explain the theoretical framework behind band alignment and how these calculations need to be adapted for Koopmans functionals. In Section III we describe the computational details and methodology that we use. Finally, in Section IV we present and discuss the electronic structure calculations of the three polymorphs and their band alignment via Koopmans functionals, and compare the results against other existing methods.

## II. THEORETICAL FRAMEWORK

As mentioned, the conduction and valence band position with respect to the water redox levels is one of the most important features of a promising photocatalyst. The positions of the band edges depend on — among other factors — the crystal structure, the chemical environment, and the surface structure of the material [35–37]. Broadly speaking, “band alignment” refers to measuring the relative alignment of the energy bands of two materials at an interface. Often this interface is between two solid materials (such as semiconductors) but it can also refer to a junction between a semiconductor and fluid (such as the case of water splitting via photocatalytic surface). There are several methods for calculating the alignment of bands at an interface, which can be broadly categorized based on the choice of reference level, or, relatedly, what system is modeled (e.g. the bulk alone vs. the explicit interface). The band alignment can be estimated from the bulk structure alone via branch point energies (BPEs) [38]. BPEs are defined as the energy points where bands change character from being predominantly donor-like to acceptor-like. It has been shown that the electronegativity and variation in

character of interface-induced gap states are determined by the nearest band edge, which can in turn be used to estimate the band offset [39]. One clear advantage of this method is that it only requires calculations of the bulk, drastically reducing its computational cost, but the method cannot be applied to materials for which the BPEs lie in the conduction band region [40]. At the other end of the spectrum, the hetero-interface can be explicitly modeled. For hetero-interfaces without lattice mismatch, this approach is straightforward because it only requires aligning the valence and conduction bands of semiconductors against the calculated average potentials in the plane parallel to the interfaces [41]. In the case of lattice mismatch, potential deformation of a core state needs to be taken into account [42, 43]. Finally, an intermediate approach is to measure the band offsets with respect to a reference level. This reference level can be the vacuum level, in which one obtains the ionization potential (IP) and electron affinity (EA) of each material [44]. These properties are intrinsically surface properties and must be obtained by considering a slab model. Alternatively, an impurity can be used as a reference level, such as hydrogen [45] or transition metal impurities [46], where band alignment relies on the position of dangling bonds formed between the impurity and semiconductor. Other more approximate approaches exist, such as effective dipole moments, tight-binding schemes, and empirical schemes [47, 48]. All of the above methods are nicely summarized in Ref. 49. In this work, we use the method based on the IP and EA of the material, adapted for use with orbital-density-dependent functionals [50–53].

### A. Band alignment with DFT

Before discussing how band alignment calculations with respect to the vacuum are performed for orbital-dependent functional theories, we first briefly review how these calculations are performed for standard functionals.

In order to calculate the ionization potential and electron affinity of a material, we must be able to reference the valence band maximum (VBM) and conduction band maximum (CBM) against the vacuum level. However, the VBM and CBM are extracted from DFT calculations as Kohn-Sham eigenvalues, whose absolute value carry no physical meaning: indeed, the Kohn-Sham potential can be shifted by an arbitrary constant leaving the physical system unchanged but shifting the KS eigenvalues by the same amount. To tether the KS eigenvalues to something meaningful, one valid choice is the potential of the vacuum. To obtain the potential in the vacuum, one considers a slab model, where the bulk catalyst is interfaced with vacuum, and then calculates the change in the average electrostatic potential between the slab and vacuum regions (denoted  $\Delta V$ ). This scheme is illustrated in Figure 2.

The average electrostatic potential is obtained by first calculating a planar average of the three-dimensional

electrostatic potential:

$$\bar{V}(z) = \frac{1}{S} \int_S dx dy V(r) \quad (3)$$

where  $S$  is the cross-sectional area of the cell parallel to the interface and for simplicity we have assumed a tetragonal cell with a slab oriented in the  $z$  direction. Within the slab region,  $\bar{V}(z)$  exhibits oscillations with a periodicity matching that of the ionic cores. These oscillations can be removed by macroscopically averaging the potential:

$$\bar{\bar{V}}(z) = \frac{1}{L} \int_{z-\frac{L}{2}}^{z+\frac{L}{2}} \bar{V}(z') dz' \quad (4)$$

using an averaging window of length  $L$  that matches the periodicity of the lattice.

Having simulated a slab model and extracted  $\Delta V$ , the vacuum level for a bulk system is then given by the average electrostatic potential across the entire cell  $\langle V \rangle_{\text{bulk}}$  plus the potential difference  $\Delta V$  as calculated from the slab calculation. The IP and EA are then given as the (negative of the) VBM and CBM energy levels relative to this vacuum level i.e.

$$\text{IP} = \Delta V - \varepsilon_{\text{VBM}} \quad (5)$$

and

$$\text{EA} = \Delta V - \varepsilon_{\text{CBM}} \quad (6)$$

We stress that this procedure relies on (a) a sufficiently thick slab, so that the electrostatic potential deep within the slab is bulk-like [54], and (b) a sufficiently wide vacuum region, in order for the electrostatic potential to converge. It is also important to allow for structural relaxation of the slab/vacuum interface as this can significantly affect the potential difference  $\Delta V$  [55].

This approach has one notable drawback: semi-local DFT eigenvalues are often not quantitatively (nor even qualitatively) accurate. It is therefore necessary to go beyond DFT to obtain accurate predictions of the valence and conduction band positions.

### B. Koopmans spectral functionals

So why are KS-DFT eigenvalues unreliable, and what can we do to improve them? To start to answer this question, we note that DFT Kohn-Sham eigenvalues do not match the corresponding energy difference one obtains from explicitly performing electron addition/removal (i.e. a  $\Delta\text{SCF}$  calculation). Contrast this with the exact one-body Green's function — an object that describes one-particle excitations *exactly* — whose excitation energies (i.e. poles) are located precisely at points that correspond to addition/removal energies (as can be straightforwardly seen from its spectral representation).

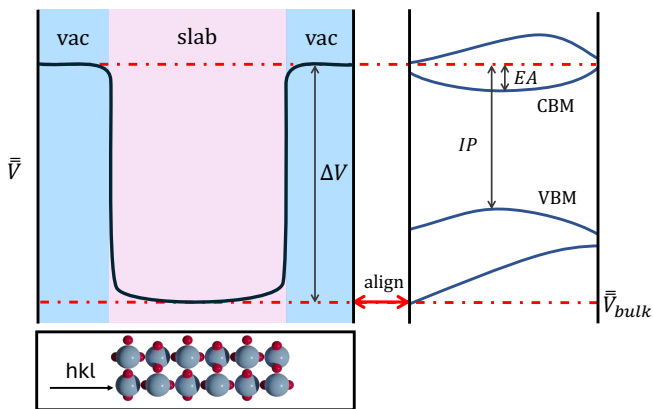


FIG. 2: Cartoon of the band alignment procedure. The black line represents the macroscopic average potential  $\Delta V$  calculated across the slab for most stable surface facet. The IP and EA correspond to the VBM and CBM relative to the vacuum reference level, which is obtained via alignment of the average potential  $V_{\text{bulk}}$  for the slab and bulk systems.

Inspired by this observation, Koopmans functionals are a class of functionals that seek to accurately describe the spectral properties of materials by restoring eigenvalue/total-energy-difference equivalence to DFT [20]. To do so, they impose the so-called “generalized piecewise-linearity” (GPWL) condition, which states that the orbital energies  $\varepsilon_i$  of orbitals  $\varphi_i$  should be inde-

pendent of that orbital’s occupation  $f_i$ :

$$\varepsilon_i = \langle \varphi_i | \hat{H} | \varphi_i \rangle = \frac{dE}{df_i} \quad (7)$$

This is related to the more well-known “piecewise linearity” (PWL) condition i.e. linearity of the total energy with respect to the total number of electrons in the system. Standard density functional approximations are not piecewise-linear, causing the aforementioned discrepancy between total energy differences and eigenvalues.

The general form of a functional that imposes the GPWL condition is:

$$E_{\text{Koopmans}}[\rho, f_i] = E^{\text{DFT}}[\rho] + \sum_i \left( - \int_0^{f_i} \varepsilon_i(f) df + f_i \eta_i \right) \quad (8)$$

As this equation shows, Koopmans functionals take the form of a correction to DFT: The first term on the right-hand side,  $E^{\text{DFT}}$ , is the energy of a (typically semi-local) “base” functional. The corrective terms then impose GPWL (equation 7) by removing, orbital-by-orbital, all non-linear dependence of the total energy on the orbital occupancies (the first term inside the parentheses) and replacing it with a term that is linear with respect to the orbital occupation  $f_i$  (the second term inside the parentheses) [56–59]. Here  $\eta_i$  is some constant. Depending on how one chooses  $\eta_i$ , different flavors of Koopmans can be defined, such as KI and KIPZ [56]. The Koopmans integral correction (KI) sets  $\eta_i$  in order to guarantee that the orbital energies  $\varepsilon_i$  are equal to the corresponding  $\Delta\text{SCF}$  total energy difference of the base functional. Explicitly, the KI functional is given by

$$E^{\text{KI}}[\{\rho_i\}] = E^{\text{DFT}}[\rho] + \sum_i \alpha_i \left[ \left( E_{\text{Hxc}}[\rho - \rho_i] - E_{\text{Hxc}}[\rho] \right) + f_i \left( E_{\text{Hxc}}[\rho - \rho_i + n_i] - E_{\text{Hxc}}[\rho - \rho_i] \right) \right] \quad (9)$$

where  $\rho_i$  is orbital density at filling  $f_i$  and  $n_i$  is the normalized orbital density i.e.  $\rho_i(\mathbf{r}) = f_i n_i(\mathbf{r})$ . The parameters  $\alpha_i$  are screening parameters, which account for the fact that the derivation of the KI correction only accounts for the explicit dependence of the DFT energy on the orbital occupancies in going from equation 8 to 9. By scaling the strength of the orbital correction via these screening parameters, we account for orbital relaxation *post hoc*. Crucially, these screening parameters  $\alpha_i$  are system-specific, and can be computed *ab initio* — i.e. they are *not* fitting parameters [60].

The second form of Koopmans functionals, KIPZ, takes the KI functional and adds one further term to the functional, a screened Perdew-Zunger (PZ) self-interaction correction term:

$$E^{\text{KIPZ}} = E^{\text{KI}} - \sum_i \alpha_i f_i E_{\text{Hxc}}[n_i] \quad (10)$$

which removes one-body self-interaction error and guarantees that the functional is exact for one-electron systems. Because evaluating the KIPZ functional is more expensive than the KI functional, it can be advantageous to evaluate the KIPZ Hamiltonian on the KI ground state. This is referred to as perturbative KIPZ (pKIPZ).

An important feature of Koopmans functionals is that they are not density functionals: the energy depends not only on the total density of the system but also on the densities of individual orbitals, making this an “orbital-density-dependent” functional theory. This comes with several important consequences. In the framework of DFT, the functional is invariant with respect to unitary rotations of the occupied manifold, and this means that the same set of orbitals minimize the total energy and diagonalize the Hamiltonian. However this is not the case for orbital-density dependent functionals, for which

the “variational” orbitals minimize the energy while the “canonical” orbitals diagonalize the Hamiltonian constructed at the end of minimization procedure. These two sets of orbitals are related via a unitary transformation.

However it is important to note that emergence of localized variational orbitals is crucial because it allows Koopmans functionals to correctly treat bulk systems [57]. The Koopmans correction is applied to each variational orbital, while the canonical orbitals are interpreted as Dyson orbitals and their eigenvalues as quasiparticle energies, which are shifted by some amount depending on the size of the Koopmans corrections applied to each of their constituent variational orbitals. In the simplest case, where all the variational orbitals are symmetrically equivalent, the Koopmans correction results in a constant shift of the valence and conduction bands, opening the band gap. For systems with non-equivalent variational orbitals the Koopmans correction also affects inter- and intra-band distances, bandwidths, effective masses, *etc.*

Because Koopmans functionals are orbital-density-dependent and have screening parameters that must be calculated *ab initio*, the procedure for computing a Koopmans band structure involves several steps as follows:

- a ground-state DFT calculation to initialize the total density
- a Wannierization of the DFT Kohn-Sham states in order to obtain maximally-localized Wannier orbitals with which to initialize the variational orbitals
- calculating the screening parameters  $\{\alpha_i\}$  via finite differences or density functional perturbation theory [61, 62]
- a final Koopmans calculation to minimize the energy and construct and diagonalize the Hamiltonian

The accuracy of Koopmans functionals has already been proven across a range of different materials [61–64]. For more details about Koopmans functionals, we refer the reader to Ref. [65].

### C. Band alignment with Koopmans functionals

To calculate band alignment with Koopmans functionals, we must adapt the procedure described earlier in Section II A. Here, we take advantage of a peculiar feature of the KI and pKIPZ functionals: for insulating systems where all the orbital occupancies are either 0 or 1, the ground state KI and pKIPZ energies and densities match those of the base functional. (This can be seen by setting  $f_i$  to 0 or 1 in equation 9). We stress that this does not mean that the Koopmans correction has no effect, because the derivative of the correction is non-vanishing and thus the eigenvalues of the Koopmans functional will

be different to those of the base functional. Nevertheless, this means that the ground-state density of Koopmans functionals match those of the base functional, and when performing band alignment the slab calculations only need to be performed at the level of DFT, because — being a ground-state property — the average electrostatic potential remains unchanged by the Koopmans correction [44, 66]. This substantially reduces the cost of this framework for computing band alignment.

Given this simplification, for Koopmans functionals equations 11 and 12 become:

$$\text{IP} = \Delta V^{\text{DFT}} - (\varepsilon_{\text{VBM}}^{\text{DFT}} + \Delta\varepsilon_{\text{VBM}}) \quad (11)$$

and

$$\text{EA} = \Delta V^{\text{DFT}} - (\varepsilon_{\text{CBM}}^{\text{DFT}} + \Delta\varepsilon_{\text{CBM}}) \quad (12)$$

where  $\Delta\varepsilon_{\text{VBM}}$  and  $\Delta\varepsilon_{\text{CBM}}$  are the shifts in these band edges due to the Koopmans correction. Equivalently, one can calculate the electron affinity (EA) by simply subtracting the value of electronic gap calculated of Koopmans level from the IP:

$$\text{EA} = \text{IP} - E_g^{\text{Koopmans}} \quad (13)$$

## III. METHOD

In this work, we present the band gaps and band alignment of three common polymorphs of  $\text{TiO}_2$ . The crystal structure of these three polymorphs were obtained from the Materials Cloud three-dimensional crystal database (MC3D) [67], which are structures whose geometries have been optimized using semi-local DFT. In the case of anatase and brookite, the optimized lattice parameters are  $a = b = 3.8001 \text{ \AA}$ , and  $c = 9.6814 \text{ \AA}$  for anatase and  $a = 5.1689 \text{ \AA}$ ,  $b = 9.2548 \text{ \AA}$ , and  $c = 5.5035 \text{ \AA}$  for brookite. They differ by less than 2% from experimentally-reported values ( $a = b = 3.7842 \text{ \AA}$  and  $c = 9.5146 \text{ \AA}$  for anatase and  $a = 5.13 \text{ \AA}$ ,  $b = 9.16 \text{ \AA}$ , and  $c = 5.43 \text{ \AA}$  for brookite). For rutile, the optimized lattice parameters are  $a = 4.60 \text{ \AA}$  and  $c = 2.96 \text{ \AA}$  (which is in excellent agreement with the experimental  $a = b = 4.5937 \text{ \AA}$  and  $c = 2.9581 \text{ \AA}$ ). There are many reported studies, both experimental and theoretical, regarding the crystal structure of  $\text{TiO}_2$  [68–74].

Koopmans functionals calculations were performed using Quantum ESPRESSO via the `koopmans` package [65, 75, 76]. The screening parameters were calculated via finite-differences, which necessitate the use of a supercell and image charge correction schemes to avoid spurious interactions between periodic images [77]. For these calculations, we used a  $2 \times 2 \times 2$  supercell for rutile and anatase and  $2 \times 1 \times 2$  supercell for brookite. To convert these  $\Gamma$ -only results to a well-sampled primitive cell the eigenvalues are unfolded to the equivalent primitive cell [63]. We used norm-conserving pseudopotentials from the SG15 library (version 1.0) [78], and a wave-function

energy cutoff of 80 Ry as recommended by force convergence data. All of the input and output files can be found on the Materials Cloud Archive [79].

For the slab calculations, we used the thermodynamically most stable facets of  $\text{TiO}_2$  polymorphs: the (110) surface facet of rutile, (101) of anatase, and (210) of brookite. These surface orientations have been extensively studied in the literature [80–88]. The slab models were constructed using six and eight periodic units for rutile and anatase, and six periodic units for the larger brookite unit cell. The depth of the vacuum was chosen to be six times the height of the bulk primitive cell (ensuring correspondence in size between primitive and supercell), which corresponds somewhere between 20 and 30 Å depending on the polymorph. These slab sizes were chosen to ensure the macroscopic average potential was converged to within 0.01 eV. The slab calculations used a  $3 \times 7 \times 1$   $k$ -point mesh for rutile and anatase and  $3 \times 2 \times 1$  for brookite. These DFT calculations were also performed using Quantum ESPRESSO. The geometries of the slab structures were optimized in order to obtain an accurate physical picture of the surface/vacuum interface.

## IV. RESULTS AND DISCUSSION

### A. Band structure

In Figure 3 we present the band structures of three polymorphs of  $\text{TiO}_2$  calculated via the KI functional, and compare them against those calculated with PBE (the underlying base functional). The band gaps of rutile and brookite  $\text{TiO}_2$  are direct ( $\Gamma \rightarrow \Gamma$ ), while that of anatase is indirect ( $Z \rightarrow \Gamma$ ) [89–91]. In all three cases, the KI correction shifts both the valence (downwards) and conduction bands (upwards), leading to the band gap widening relative to the PBE result. (The precise values of these shifts can be found in the Supplemental Material.) The resulting band gaps are presented in Table I, alongside experimental values, as well as those calculated using hybrid functionals and GW. When comparing against experimental band gaps it is important to account for zero-point renormalization — by subtracting the ZPR (as calculated *ab initio*) from experimental values one obtains a value that can be fairly compared against the computational results obtained for pristine crystal geometries.

For rutile and anatase, the electronic band gaps calculated using KI@PBE are within 0.36 eV of experiment (when accounting for ZPR). This level of accuracy is a drastic improvement on that of the base functional PBE, is comparable to that of  $\text{G}_0\text{W}_0$ @PBE and hybrid functionals, and is better than  $\text{G}_0\text{W}_0$ @HSE06 and self-consistent quasiparticle GW. For brookite, no ZPR correction was found in the literature and thus comparison with experiment is not possible.

TABLE I: Electronic band gaps (in eV) of  $\text{TiO}_2$  polymorphs at different levels of theory.

	rutile	anatase	brookite
PBE	1.73	2.21	2.42
HSE06 <sup>ab</sup>	3.39, 3.61	3.60	3.30
$\text{G}_0\text{W}_0$ @PBE <sup>a</sup>	3.46	3.73	3.45
$\text{G}_0\text{W}_0$ @HSE06 <sup>b</sup>	4.73	—	—
scQPGW@HSE06 <sup>b</sup>	5.18	—	—
KI@PBE	3.29	3.80	4.03
pKIPZ@PBE	3.38	3.90	4.14
exp – ZPR	3.34 – 3.41	3.34 – 3.44	—
exp <sup>c</sup>	3.03 – 3.06	3.10 – 3.20	3.1 – 3.4
ZPR <sup>d</sup>	–0.337, –0.349, –0.314	–0.238	—

<sup>a</sup> [92]

<sup>b</sup> [33]

<sup>c</sup> [93–95]

<sup>d</sup> [96–98]

The results with pKIPZ are very similar to that of KI (plots of pKIPZ@PBE band structures can be found in the Supplemental Material). Compared to the KI functional, pKIPZ reports slightly larger band gaps, especially in the case of brookite. Both KI and pKIPZ assign brookite the largest band gap of the three polymorphs, in contrast to HSE06 and  $\text{G}_0\text{W}_0$ @PBE which assign it the smallest. But without an accurate measurement of the ZPR in brookite and more precise experimental measurements of the band gap, it is difficult to determine which ordering is correct.

### B. Band alignment

The ionization potentials and electron affinities of the  $\text{TiO}_2$  polymorphs, as calculated via KI and pKIPZ following the method described in Section II C, are reported in Table II alongside values obtained from other higher levels of theory and experiment. Once again it is important to account for ZPR when comparing against experiment. However, ZPR shifts for the VBM and CBM individually have only been reported for the rutile polymorph, calculated using a generalized Fröhlich model [101]. This technique is more approximate than those that were used to calculate the ZPR shifts in the band gaps listed in Table I. Note that the combining the shifts for the VBM and CBM predicted by the Fröhlich model results in a ZPR reduction of the band gap (0.47 eV) that is up to 50% larger than those listed in Table I, so these results should be treated with caution.

That caveat aside, for rutile KI@PBE underestimates the shifted experimental IP by 0.5 eV — comparable to the accuracy of  $\text{G}_0\text{W}_0$ @HSE06. The EA, on the other hand, is predicted by KI@PBE within the range of values reported experimentally — a marked improvement upon

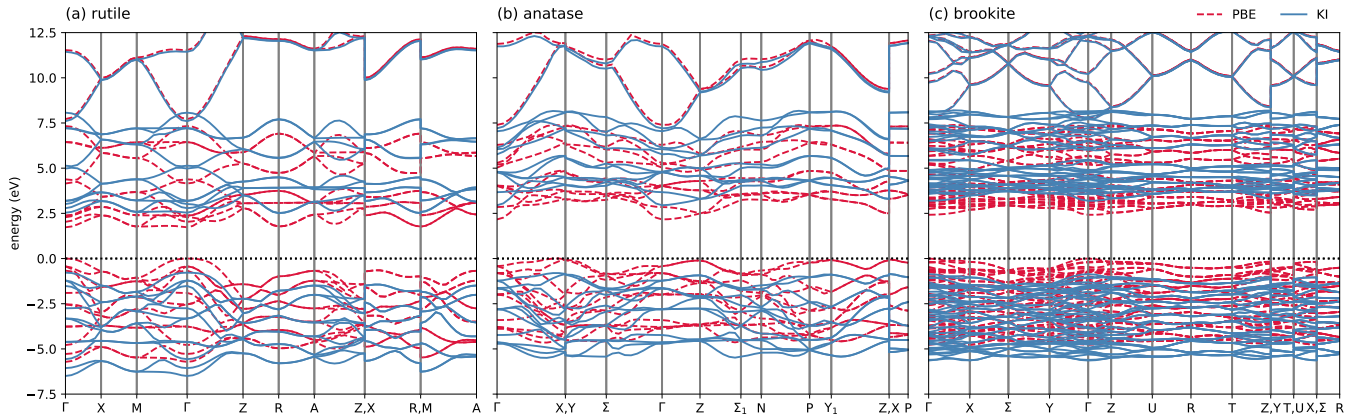


FIG. 3: KI@PBE band structures (blue) with respect to the PBE bands (red); the zero reference energy is set to  $\epsilon_{\text{VBM}}^{\text{DFT}}$ .

TABLE II: Ionization potentials and electron affinities in eV obtained on KI and pKIPZ level in comparison with experimental studies of single-crystal polymorphs.

	rutile (110)		anatase (101)		brookite (210)	
	IP	EA	IP	EA	IP	EA
PBE	7.22	5.55	7.11	4.90	7.17	4.78
HSE06 <sup>a</sup>	8.66	4.99	—	—	—	—
HSE06 (QM/MM) <sup>b</sup>	7.83	—	8.3	—	—	—
G <sub>0</sub> W <sub>0</sub> @PBE <sup>a</sup>	7.29	3.03	—	—	—	—
G <sub>0</sub> W <sub>0</sub> @HSE06 <sup>a</sup>	7.92	3.19	—	—	—	—
scQPGW@HSE06 <sup>a</sup>	8.77	3.59	—	—	—	—
KI@PBE	8.00	4.71	8.19	4.39	8.03	4.00
pKIPZ@PBE	7.83	4.44	8.00	4.10	7.84	3.71
exp – ZPR	8.5	4.97 – 5.00	—	—	—	—
exp <sup>c</sup>	8.20	5.14 – 5.17	7.96, 8.07, 8.20	—	—	—
ZPR <sup>d</sup>	-0.3	0.17	—	—	—	—

<sup>a</sup> [33]

<sup>b</sup> [36]

<sup>c</sup> [80, 99, 100]

<sup>d</sup> [101]

the GW results, and matched only by HSE06.

For anatase and brookite, no ZPR results for the IP and EA were found. The KI and pKIPZ result for the IP of anatase are fractionally lower than that given by HSE06 [36].

The band alignment diagram represented in Figure 4 shows the IPs and EAs of the three polymorphs compared against the two redox reaction potentials. The  $\text{H}^+/\text{H}_2$  potential lies at -4.44 eV [102], while the  $\text{H}_2\text{O}/\text{O}_2$  potential is 1.23 eV below this (as per Equation 1) [8]. The positions of the valence and conduction bands should straddle these two potentials i.e. the VBM and CBM should not lie within the two dashed lines in Figure 4. According to our calculations, rutile  $\text{TiO}_2$  appears not to satisfy this condition, which may explain why — despite having a more desirable band gap than anatase and brookite — this polymorph is a slightly worse catalyst,

especially compared to anatase [103]. (Of course, an optimal band alignment does not guarantee photocatalytic success: anatase also exhibits higher surface activity and desirable excitonic properties [103, 104].) Brookite, on the other hand, shows some promise as a photocatalyst: the positions of the valence and the conduction bands seem to be favorable, but its fractionally larger band gap would limit the amount of photons that would be absorbed when subjected to sunlight. In this case, one might be able to engineer the band gap.

The KI and pKIPZ results are qualitatively the same, with pKIPZ reporting a slightly more favorable CBM for rutile relative to the hydrogen reduction reaction. Still, with respect to the value of band gap and band edge positions, both KI and pKIPZ predict that anatase appears to be the most promising photocatalyst of the three.



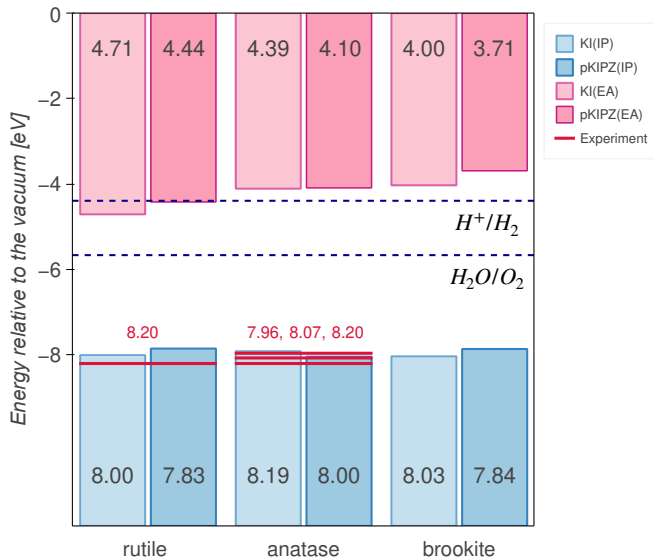


FIG. 4: Band alignment of TiO<sub>2</sub> polymorphs using KI and pKIPZ. Blue rectangles represent the IPs of three polymorphs, while red rectangles the EAs. Experimental values are given as red solid lines (from Refs. [57, 80, 99, 100]).

## V. CONCLUSIONS

In conclusion, this investigation demonstrates the accuracy of Koopmans spectral functionals for calculating the band gap, IP, and EAs of TiO<sub>2</sub>, finding — in agreement with experiment — that anatase is the most promising photocatalyst of the three. The individual predictions of the ionization potentials and electron affinities were either as or more accurate than the results of hybrid functionals and many-body perturbation theory. At the same time, the band alignment calculations presented in this work are notably simpler, given that this framework only requires Koopmans functional calculations on the primitive cell and semi-local DFT calculations for the slab calculations. In the future, Koopmans functionals could be deployed to screen promising photocatalyst candidates that are much less well-studied.

## VI. ACKNOWLEDGMENTS

MS acknowledges support from EXAF (Excellence in Africa) Research Centre as part of the collaboration “Embedded exact quantum dynamics for photocatalytic water splitting”. This research was supported by the NCCR MARVEL, a National Centre of Competence in Research, funded by the Swiss National Science Foundation (grant number 205602).

\* marija.stojkovic@epfl.ch

- [1] A. Fujishima and K. Honda, Electrochemical photolysis of water at a semiconductor electrode, *Nature* **238**, 37 (1972).
- [2] A. Kudo and Y. Miseki, Heterogeneous photocatalyst materials for water splitting, *Chem. Soc. Rev.* **38**, 253 (2009).
- [3] M. Ni, M. K. Leung, D. Y. Leung, and K. Sumathy, A review and recent developments in photocatalytic water-splitting using TiO<sub>2</sub> for hydrogen production, *Renew. Sustain. Energy Rev.* **11**, 401 (2007).
- [4] K. Maeda and K. Domen, Photocatalytic water splitting: Recent progress and future challenges, *J. Phys. Chem. Lett.* **1**, 2655 (2010).
- [5] K. Takanabe, Photocatalytic water splitting: Quantitative approaches toward photocatalyst by design, *ACS Catal.* **7**, 8006 (2017).
- [6] L. Yang, H. Zhou, T. Fan, and D. Zhang, Semiconductor photocatalysts for water oxidation: Current status and challenges, *Phys. Chem. Chem. Phys.* **16**, 6810 (2014).
- [7] C.-F. Fu, X. Wu, and J. Yang, Material design for photocatalytic water splitting from a theoretical perspective, *Adv. Mater.* **30**, 1802106 (2018).
- [8] J. Rumble, *CRC Handbook of Chemistry and Physics*, 105th ed. (CRC Press, Taylor & Francis Group, 2023).
- [9] T. Jafari, E. Moharreri, A. S. Amin, R. Miao, W. Song, and S. L. Suib, Photocatalytic water splitting—the untamed dream: A review of recent advances, *Molecules* **21**, 900 (2016).
- [10] M. G. Walter, E. L. Warren, J. R. McKone, S. W. Boettcher, Q. Mi, E. A. Santori, and N. S. Lewis, Solar water splitting cells, *Chem. Rev.* **110**, 6446 (2010).
- [11] K.-W. Park and A. M. Kolpak, Mechanism for spontaneous oxygen and hydrogen evolution reactions on CoO nanoparticles, *J. Mater. Chem. A* **7**, 6708 (2019).
- [12] M. K. Harbola, Relationship between the highest occupied Kohn-Sham orbital eigenvalue and ionization energy, *Phys. Rev. B* **60**, 4545 (1999).
- [13] A. Grüneis, G. Kresse, Y. Hinuma, and F. Oba, Ionization potentials of solids: The importance of vertex corrections, *Phys. Rev. Lett.* **112**, 096401 (2014).
- [14] J. P. Perdew and A. Zunger, Self-interaction correction to density-functional approximations for many-electron systems, *Phys. Rev. B* **23**, 5048 (1981).
- [15] H. J. Kulik, M. Cococcioni, D. A. Scherlis, and N. Marzari, Density functional theory in transition-metal chemistry: A self-consistent Hubbard *u* approach, *Phys. Rev. Lett.* **97**, 103001 (2006).
- [16] J. P. Perdew, R. G. Parr, M. Levy, and J. L. Balduz Jr, Density-functional theory for fractional particle number: Derivative discontinuities of the energy, *Phys. Rev. Lett.* **49**, 1691 (1982).
- [17] A. J. Cohen, P. Mori-Sánchez, and W. Yang, Challenges for density functional theory, *Chem. Rev.* **112**, 289 (2012).
- [18] P. Mori-Sánchez, A. J. Cohen, and W. Yang, Localization and delocalization errors in density functional theory and implications for band-gap prediction, *Phys.*



- Rev. Lett. **100**, 146401 (2008).
- [19] L. Kronik and S. Kümmel, Piecewise linearity, freedom from self-interaction, and a coulomb asymptotic potential: three related yet inequivalent properties of the exact density functional, Phys. Chem. Chem. Phys. **22**, 16467 (2020).
- [20] I. Dabo, A. Ferretti, N. Poilvert, Y. Li, N. Marzari, and M. Cococcioni, Koopmans' condition for density-functional theory, Phys. Rev. B **82**, 115121 (2010).
- [21] M. Cococcioni and S. de Gironcoli, Linear response approach to the calculation of the effective interaction parameters in the LDA + U method, Phys. Rev. B **71**, 035105 (2005).
- [22] M. K. Harbola, Relationship between the highest occupied Kohn-Sham orbital eigenvalue and ionization energy, Phys. Rev. B **60**, 4545 (1999).
- [23] J. Heyd, G. E. Scuseria, and M. Ernzerhof, Hybrid functionals based on a screened Coulomb potential, J. Chem. Phys. **118**, 8207 (2003).
- [24] M. Marsman, J. Paier, A. Stroppa, and G. Kresse, Hybrid functionals applied to extended systems, J. Phys. Condens. Matter **20**, 064201 (2008).
- [25] AD. Becke, A half-half theory of density functionals, J. Chem. Phys. **98**, 1372 (1993).
- [26] E. Kraisler, Asymptotic behavior of the exchange-correlation energy density and the kohn-sham potential in density functional theory: Exact results and strategy for approximations, Isr. J. Chem. **60**, 805 (2020).
- [27] B. Himmetoglu, A. Floris, S. De Gironcoli, and M. Cococcioni, Hubbard-corrected DFT energy functionals: The LDA+ U description of correlated systems, Int. J. Quantum Chem. **114**, 14 (2014).
- [28] V. L. Campo and M. Cococcioni, Extended DFT + U + V method with on-site and inter-site electronic interactions, J. Phys.: Condens. Matter **22**, 055602 (2010).
- [29] F. Aryasetiawan and O. Gunnarsson, The GW method, Rep. Prog. Phys. **61**, 237 (1998).
- [30] M. Shishkin and G. Kresse, Implementation and performance of the frequency-dependent G W method within the PAW framework, Phys. Rev. B **74**, 035101 (2006).
- [31] D. Golze, M. Dvorak, and P. Rinke, The GW compendium: A practical guide to theoretical photoemission spectroscopy, Front. Chem. **7**, 377 (2019).
- [32] C. Mitra, B. Lange, C. Freysoldt, and J. Neugebauer, Quasiparticle band offsets of semiconductor heterojunctions from a generalized marker method, Phys. Rev. B **84**, 193304 (2011).
- [33] A. Migani, D. J. Mowbray, J. Zhao, H. Petek, and A. Rubio, Quasiparticle level alignment for photocatalytic interfaces, J. Chem. Theory Comput. **10**, 2103 (2014).
- [34] Z. Hiroi, Inorganic structural chemistry of titanium dioxide polymorphs, Inorg. Chem. **61**, 8393 (2022).
- [35] K.-W. Park and A. M. Kolpak, Optimal methodology for explicit solvation prediction of band edges of transition metal oxide photocatalysts, Commun. Chem. **2**, 1 (2019).
- [36] D. O. Scanlon, C. W. Dunnill, J. Buckeridge, S. A. Shevlin, A. J. Logsdail, S. M. Woodley, C. R. A. Catlow, M. Powell, R. G. Palgrave, I. P. Parkin, *et al.*, Band alignment of rutile and anatase TiO<sub>2</sub>, Nat. Mater. **12**, 798 (2013).
- [37] V. Pfeifer, P. Erhart, S. Li, K. Rachut, J. Morasch, J. Brötz, P. Reckers, T. Mayer, S. Rühle, A. Zaban, *et al.*, Energy band alignment between anatase and rutile TiO<sub>2</sub>, J. Phys. Chem. Lett. **4**, 4182 (2013).
- [38] J. Tersoff, Schottky barrier heights and the continuum of gap states, Phys. Rev. Lett. **52**, 465 (1984).
- [39] W. Mönch, Elementary calculation of the branch-point energy in the continuum of interface-induced gap states, Appl. Surf. Sci. **117–118**, 380 (1997).
- [40] Branch-point energies and band discontinuities of III-nitrides and III-/II-oxides from quasiparticle band-structure calculations, Appl. Phys. Lett. **94** (2009).
- [41] C. G. Van de Walle and R. M. Martin, Theoretical study of band offsets at semiconductor interfaces, Phys. Rev. B **35**, 8154 (1987).
- [42] Y.-H. Li, X. G. Gong, and S.-H. Wei, Ab initio all-electron calculation of absolute volume deformation potentials of IV-IV, III-V, and II-VI semiconductors: The chemical trends, Phys. Rev. B **73**, 245206 (2006).
- [43] A. Franceschetti, S.-H. Wei, and A. Zunger, Absolute deformation potentials of al, si, and NaCl, Phys. Rev. B **50**, 17797 (1994).
- [44] V. Stevanović, S. Lany, D. S. Ginley, W. Tumas, and A. Zunger, Assessing capability of semiconductors to split water using ionization potentials and electron affinities only, Phys. Chem. Chem. Phys. **16**, 3706 (2014).
- [45] C. G. Van de Walle and J. Neugebauer, Universal alignment of hydrogen levels in semiconductors, insulators and solutions, Nature **423**, 626 (2003).
- [46] J. M. Langer, C. Delerue, M. Lannoo, and H. Heinrich, Transition-metal impurities in semiconductors and heterojunction band lineups, Phys. Rev. B **38**, 7723 (1988).
- [47] J. C. Conesa, Computing with DFT band offsets at semiconductor interfaces: A comparison of two methods, Nanomaterials **11**, 10.3390/nano11061581 (2021).
- [48] J. Tersoff, Theory of semiconductor heterojunctions: The role of quantum dipoles, Phys. Rev. B **30**, 4874 (1984).
- [49] Y. Hinuma, A. Grüneis, G. Kresse, and F. Oba, Band alignment of semiconductors from density-functional theory and many-body perturbation theory, Phys. Rev. B **90**, 155405 (2014).
- [50] W. Kang and M. S. Hybertsen, Quasiparticle and optical properties of rutile and anatase TiO<sub>2</sub>, Phys. Rev. B **82**, 085203 (2010).
- [51] W.-J. Yin, H. Tang, S.-H. Wei, M. M. Al-Jassim, J. Turner, and Y. Yan, Band structure engineering of semiconductors for enhanced photoelectrochemical water splitting: The case of TiO<sub>2</sub>, Phys. Rev. B **82**, 045106 (2010).
- [52] R. Shaltaf, G.-M. Rignanese, X. Gonze, F. Giustino, and A. Pasquarello, Band offsets at the Si/SiO<sub>2</sub> interface from many-body perturbation theory, Phys. Rev. Lett. **100**, 186401 (2008).
- [53] Y. Wu, M.K.Y. Chan, and G. Ceder, Prediction of semiconductor band edge positions in aqueous environments from first principles, Phys. Rev. B **83**, 235301 (2011).
- [54] C. G. Van de Walle and R. M. Martin, Theoretical study of band offsets at semiconductor interfaces, Phys. Rev. B **35**, 8154 (1987).
- [55] L. Weston, H. Taylor, K. Krishnaswamy, L. Bjaalie, and CG. Van de Walle, Accurate and efficient band-offset calculations from density functional theory, Comput. Mater. Sci. **151**, 174 (2018).

- [56] N. L. Nguyen, G. Borghi, A. Ferretti, I. Dabo, and N. Marzari, First-principles photoemission spectroscopy and orbital tomography in molecules from Koopmans-compliant functionals, *Phys. Rev. Lett.* **114**, 166405 (2015).
- [57] N. L. Nguyen, N. Colonna, A. Ferretti, and N. Marzari, Koopmans-compliant spectral functionals for extended systems, *Phys. Rev. X* **8**, 021051 (2018).
- [58] G. Borghi, A. Ferretti, N. L. Nguyen, I. Dabo, and N. Marzari, Koopmans-compliant functionals and their performance against reference molecular data, *Phys. Rev. B* **90**, 075135 (2014).
- [59] G. Borghi, C.-H. Park, N. L. Nguyen, A. Ferretti, and N. Marzari, Variational minimization of orbital-density-dependent functionals, *Phys. Rev. B* **91**, 155112 (2015).
- [60] N. Colonna, N. L. Nguyen, A. Ferretti, and N. Marzari, Screening in Orbital-Density-Dependent Functionals, *J. Chem. Theory Comput.* **14**, 2549 (2018).
- [61] N. Colonna, N. L. Nguyen, A. Ferretti, and N. Marzari, Koopmans-compliant functionals and potentials and their application to the GW100 test set, *J. Chem. Theory Comput.* **15**, 1905 (2019).
- [62] N. Colonna, R. De Gennaro, E. Linscott, and N. Marzari, Koopmans spectral functionals in periodic boundary conditions, *J. Chem. Theory Comput.* **18**, 5435 (2022).
- [63] R. De Gennaro, N. Colonna, E. Linscott, and N. Marzari, Bloch's theorem in orbital-density-dependent functionals: Band structures from Koopmans spectral functionals, *Phys. Rev. B* **106**, 035106 (2022).
- [64] A. Marrazzo and N. Colonna, Spin-dependent interactions in orbital-density-dependent functionals: Non-collinear Koopmans spectral functionals, *Phys. Rev. Res.* **6**, 033085 (2024).
- [65] E. B. Linscott, N. Colonna, R. De Gennaro, N. L. Nguyen, G. Borghi, A. Ferretti, I. Dabo, and N. Marzari, Koopmans: An open-source package for accurately and efficiently predicting spectral properties with Koopmans functionals, *J. Chem. Theory Comput.* **19**, 7097 (2023).
- [66] R. Shaltaf, G.-M. Rignanese, X. Gonze, F. Giustino, and A. Pasquarello, Band offsets at the Si/SiO<sub>2</sub> interface from many-body perturbation theory, *Phys. Rev. Lett.* **100**, 186401 (2008).
- [67] S. P. Huber, M. Berx, N. Hörmann, M. Uhrin, G. Pizzi, and N. Marzari, Materials Cloud three-dimensional crystals database (MC3D) (2022).
- [68] DG. Isaak, JD. Carnes, OL. Anderson, H. Cynn, and E. Hake, Elasticity of TiO<sub>2</sub> rutile to 1800 K, *Phys. Chem. Miner.* **26**, 31 (1998).
- [69] R. Asahi, Y. Taga, W. Mannstadt, and A. J. Freeman, Electronic and optical properties of anatase TiO<sub>2</sub>, *Phys. Rev. B* **61**, 7459 (2000).
- [70] R. S. Dima, L. Phuthu, N. E. Maluta, J. K. Kirui, and R. R. Maphanga, Electronic, structural, and optical properties of mono-doped and Co-Doped (210) TiO<sub>2</sub> brookite surfaces for application in dye-sensitized solar cells—a first principles study, *Materials* **14**, 3918 (2021).
- [71] S. Banerjee, A. Zangiabadi, A. Mahdavi-Shakib, S. Husremovic, B. G. Frederick, K. Barmak, R. N. Austin, and S. J. Billinge, Quantitative structural characterization of catalytically active TiO<sub>2</sub> nanoparticles, *ACS Appl. Nano Mater.* **2**, 6268 (2019).
- [72] J. K. Burdett, T. Hughbanks, G. J. Miller, J. W. Richardson Jr, and J. V. Smith, Structural-electronic relationships in inorganic solids: Powder neutron diffraction studies of the rutile and anatase polymorphs of titanium dioxide at 15 and 295 K, *J. Am. Chem. Soc.* **109**, 3639 (1987).
- [73] T. Mashimo, R. Bagum, Y. Ogata, M. Tokuda, M. Okube, K. Sugiyama, Y. Kinemuchi, H. Isobe, and A. Yoshiasa, Structure of single-crystal rutile TiO<sub>2</sub> prepared by high-temperature ultracentrifugation, *Cryst. Growth Des.* **17**, 1460 (2017).
- [74] M. Gateshki, S. Yin, Y. Ren, and V. Petkov, Titania polymorphs by soft chemistry: Is there a common structural pattern?, *Chem. Mater.* **19**, 2512 (2007).
- [75] P. Giannozzi, S. Baroni, N. Bonini, M. Calandra, R. Car, C. Cavazzoni, D. Ceresoli, G. L. Chiarotti, M. Cococcioni, I. Dabo, *et al.*, QUANTUM ESPRESSO: A modular and open-source software project for quantum simulations of materials, *J. Phys. Condens. Matter* **21**, 395502 (2009).
- [76] P. Giannozzi, O. Andreussi, T. Brumme, O. Bunau, M. B. Nardelli, M. Calandra, R. Car, C. Cavazzoni, D. Ceresoli, M. Cococcioni, N. Colonna, I. Carnimeo, A. D. Corso, S. de Gironcoli, P. Delugas, R. A. DiStasio, A. Ferretti, A. Floris, G. Fratesi, G. Fugallo, R. Gebauer, U. Gerstmann, F. Giustino, T. Gorni, J. Jia, M. Kawamura, H.-Y. Ko, A. Kokalj, E. Küçükbenli, M. Lazzeri, M. Marsili, N. Marzari, F. Mauri, N. L. Nguyen, H.-V. Nguyen, A. Otero-de-la-Roza, L. Paulatto, S. Poncé, D. Rocca, R. Sabatini, B. Santra, M. Schlipf, A. P. Seitsonen, A. Smogunov, I. Timrov, T. Thonhauser, P. Umari, N. Vast, X. Wu, and S. Baroni, Advanced capabilities for materials modelling with Quantum ESPRESSO, *J. Phys. Condens. Matter* **29**, 465901 (2017).
- [77] G. J. Martyna and M. E. Tuckerman, A reciprocal space based method for treating long range interactions in ab initio and force-field-based calculations in clusters, *J. Chem. Phys.* **110**, 2810 (1999).
- [78] P. Scherpelz, M. Govoni, I. Hamada, and G. Galli, Implementation and validation of fully relativistic GW calculations: Spin-orbit coupling in molecules, nanocrystals, and solids, *J. Chem. Theory Comput.* **12**, 3523 (2016).
- [79] M. Stojkovic, E. Linscott, and N. Marzari, Predicting the suitability of photocatalysts for water splitting using Koopmans spectral functionals: The case of TiO<sub>2</sub> polymorphs (2024).
- [80] AG. Thomas, WR. Flavell, AR. Kumarasinghe, AK. Mallick, D. Tsoutsou, GC. Smith, R. Stockbauer, S. Patel, M. Grätzel, and R. Hengerer, Resonant photoemission of anatase TiO<sub>2</sub> (101) and (001) single crystals, *Phys. Rev. B* **67**, 035110 (2003).
- [81] S. Wendt, J. Matthesen, R. Schaub, E. K. Vestergaard, E. Lægsgaard, F. Besenbacher, and B. Hammer, Formation and splitting of paired hydroxyl groups on reduced TiO<sub>2</sub> (110), *Phys. Rev. Lett.* **96**, 066107 (2006).
- [82] U. Martinez, L. B. Vilhelmsen, H. H. Kristoffersen, J. Stausholm Møller, and B. Hammer, Steps on rutile TiO<sub>2</sub> (110): Active sites for water and methanol dissociation, *Phys. Rev. B* **84**, 205434 (2011).
- [83] M. Lazzeri, A. Vittadini, and A. Selloni, Structure and energetics of stoichiometric TiO<sub>2</sub> anatase surfaces, *Phys. Rev. B* **63**, 155409 (2001).

- [84] U. Diebold, N. Ruzycki, G. S. Herman, and A. Selloni, One step towards bridging the materials gap: Surface studies of TiO<sub>2</sub> anatase, *Catal. Today* **85**, 93 (2003).
- [85] R. Hengerer, B. Bolliger, M. Erbudak, and M. Grätzel, Structure and stability of the anatase TiO<sub>2</sub>(101) and (001) surfaces, *Surf. Sci.* **460**, 162 (2000).
- [86] A. Y. Ahmed, T. A. Kandiel, T. Oekermann, and D. Bahnemann, Photocatalytic activities of different well-defined single crystal TiO<sub>2</sub> surfaces: Anatase versus rutile, *J. Phys. Chem. Lett.* **2**, 2461 (2011).
- [87] F. De Angelis, C. Di Valentin, S. Fantacci, A. Vittadini, and A. Selloni, Theoretical studies on anatase and less common TiO<sub>2</sub> phases: Bulk, surfaces, and nanomaterials, *Chem. Rev.* **114**, 9708 (2014).
- [88] JØ. Hansen, P. Huo, U. Martinez, E. Lira, YY. Wei, R. Streber, E. Lægsgaard, B. Hammer, S. Wendt, and F. Besenbacher, Direct evidence for ethanol dissociation on rutile TiO<sub>2</sub> (110), *Phys. Rev. Lett.* **107**, 136102 (2011).
- [89] P. Deak, B. Aradi, and T. Frauenheim, Band lineup and charge carrier separation in mixed rutile-anatase systems, *J. Phys. Chem. C* **115**, 3443 (2011).
- [90] D. Zhang and S. Dong, Challenges in band alignment between semiconducting materials: A case of rutile and anatase TiO<sub>2</sub>, *Prog. Nat. Sci. Mater. Int.* **29**, 277 (2019).
- [91] M. Manzoli, F. S. Freyria, N. Blangetti, and B. Bonelli, Brookite, a sometimes under evaluated TiO<sub>2</sub> polymorph, *RSC Adv.* **12**, 3322 (2022).
- [92] M. Landmann, EWGS. Rauls, and WG. Schmidt, The electronic structure and optical response of rutile, anatase and brookite TiO<sub>2</sub>, *J. Phys. Condens. Matter* **24**, 195503 (2012).
- [93] J. Zhang, P. Zhou, J. Liu, and J. Yu, New understanding of the difference of photocatalytic activity among anatase, rutile and brookite TiO<sub>2</sub>, *Phys. Chem. Chem. Phys.* **16**, 20382 (2014).
- [94] G. Xiong, R. Shao, T. C. Droubay, A. G. Joly, K. M. Beck, S. A. Chambers, and W. P. Hess, Photoemission electron microscopy of TiO<sub>2</sub> anatase films embedded with rutile nanocrystals, *Adv. Funct. Mater.* **17**, 2133 (2007).
- [95] R. S. Dima, L. Phuthu, N. E. Maluta, J. K. Kirui, and R. R. Maphanga, Electronic, structural, and optical properties of mono-doped and co-doped (210) TiO<sub>2</sub> brookite surfaces for application in dye-sensitized solar cells—a first principles study, *Materials* **14**, 10.3390/ma14143918 (2021).
- [96] A. Miglio, V. Brousseau-Couture, E. Godbout, G. Antonius, Y.-H. Chan, S. G. Louie, M. Côté, M. Giantomassi, and X. Gonze, Predominance of non-adiabatic effects in zero-point renormalization of the electronic band gap, *Npj Comput. Mater.* **6**, 167 (2020).
- [97] M. Engel, H. Miranda, L. Chaput, A. Togo, C. Verdi, M. Marsman, and G. Kresse, Zero-point renormalization of the band gap of semiconductors and insulators using the projector augmented wave method, *Phys. Rev. B* **106**, 094316 (2022).
- [98] Y.-N. Wu, J. K. Wuenschell, R. Fryer, W. A. Saidi, P. Ohodnicki, B. Chorpening, and Y. Duan, Theoretical and experimental study of temperature effect on electronic and optical properties of TiO<sub>2</sub>: Comparing rutile and anatase, *J. Phys.: Condens. Matter* **32**, 405705 (2020).
- [99] S. Kashiwaya, J. Morasch, V. Streibel, T. Toupance, W. Jaegermann, and A. Klein, The work function of TiO<sub>2</sub>, *Surfaces* **1**, 73 (2018).
- [100] AG. Thomas, WR. Flavell, AK. Mallick, AR. Kumarasinghe, D. Tsoutsou, N. Khan, C. Chatwin, S. Rayner, GC. Smith, RL. Stockbauer, *et al.*, Comparison of the electronic structure of anatase and rutile TiO<sub>2</sub> single-crystal surfaces using resonant photoemission and x-ray absorption spectroscopy, *Phys. Rev. B* **75**, 035105 (2007).
- [101] P. M. M. C. de Melo, J. C. de Abreu, B. Guster, M. Giantomassi, Z. Zanolli, X. Gonze, and M. J. Verstraete, High-throughput analysis of Fröhlich-type polaron models, *npj Comput Mater* **9**, 1 (2023).
- [102] S. Trasatti, The absolute electrode potential: an explanatory note (recommendations 1986), *Pure and Applied Chemistry* **58**, 955 (1986).
- [103] T. Luttrell, S. Halpegamage, J. Tao, A. Kramer, E. Sutter, and M. Batzill, Why is anatase a better photocatalyst than rutile?—Model studies on epitaxial TiO<sub>2</sub> films, *Sci. Rep.* **4**, 4043 (2014).
- [104] H. Eidsvåg, S. Bentouba, P. Vajeeston, S. Yohi, and D. Velauthapillai, TiO<sub>2</sub> as a photocatalyst for water splitting—An experimental and theoretical review, *Molecules* **26**, 1687 (2021).

**Supplemental Material for: Predicting the suitability of  
photocatalysts for water splitting using Koopmans spectral  
functionals: The case of TiO<sub>2</sub> polymorphs**

Marija Stojkovic,<sup>1,\*</sup> Edward Linscott,<sup>2,3</sup> and Nicola Marzari<sup>1,2,3</sup>

<sup>1</sup>*Theory and Simulations of Materials (THEOS),*

*École Polytechnique Fédérale de Lausanne, 1015 Lausanne, Switzerland*

<sup>2</sup>*Center for Scientific Computing, Theory and Data,*

*Paul Scherrer Institute, 5232 Villigen PSI, Switzerland*

<sup>3</sup>*National Centre for Computational Design and Discovery of Novel Materials (MARVEL),*

*Paul Scherrer Institute, 5232 Villigen PSI, Switzerland*

(Dated: December 24, 2024)

TABLE S1: VBM and CBM of three polymorphs of TiO<sub>2</sub> obtained using semi-local DFT (PBE) and two flavors of Koopmans functionals (KI and pKIPZ). All values are given in units of eV.

	HOMO			LUMO			$\Delta VBM$		$\Delta CBM$	
	PBE	KI	pKIPZ	PBE	KI	pKIPZ	KI	pKIPZ	KI	pKIPZ
rutile	-0.55	-1.33	-1.16	1.18	1.96	2.22	-0.78	-0.61	0.78	1.04
anatase	-1.65	-2.46	-2.27	0.56	1.34	1.63	-0.81	-0.62	0.78	1.07
brookite	-1.17	-2.03	-1.84	1.25	2.00	2.29	-0.86	-0.67	0.75	1.04

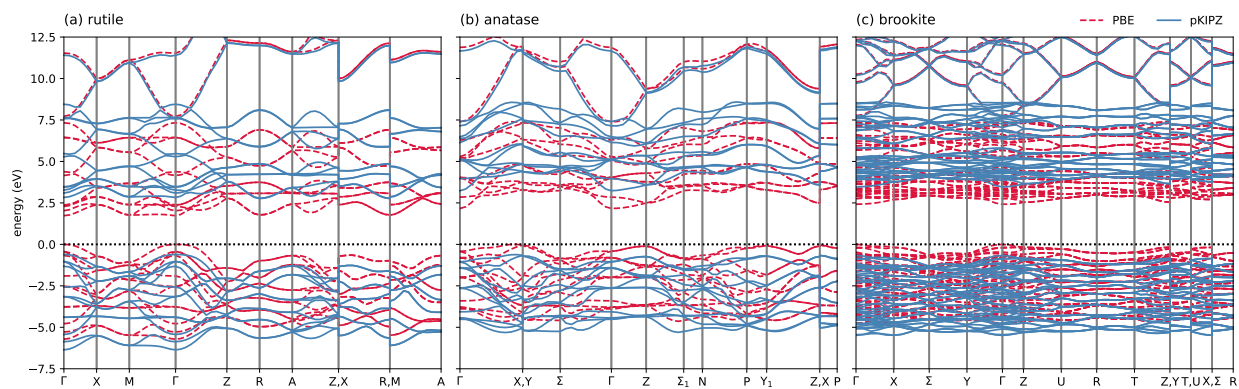


FIG. S1: pKIPZ band structures of three polymorphs of  $\text{TiO}_2$ , alongside the PBE bands, with the reference energy set to  $\epsilon_{\text{VBM}}^{\text{DFT}}$ .